



Title	Chemically Controlled Volatile and Nonvolatile Resistive Memory Characteristics of Novel Oxygen-Based Polymers
Author(s)	Ree, Brian J.; Isono, Takuya; Satoh, Toshifumi
Citation	ACS applied materials & interfaces, 12(25), 28435-28445 <a href="https://doi.org/10.1021/acsami.0c06939">https://doi.org/10.1021/acsami.0c06939</a>
Issue Date	2020-06-24
Doc URL	<a href="http://hdl.handle.net/2115/82012">http://hdl.handle.net/2115/82012</a>
Rights	This document is the Accepted Manuscript version of a Published Work that appeared in final form in ACS applied materials & interfaces, copyright c American Chemical Society after peer review and technical editing by the publisher. To access the final edited and published work see <a href="https://pubs.acs.org/doi/10.1021/acsami.0c06939">https://pubs.acs.org/doi/10.1021/acsami.0c06939</a> .
Type	article (author version)
Additional Information	There are other files related to this item in HUSCAP. Check the above URL.
File Information	BJR-manuscript-1-1.pdf



[Instructions for use](#)

# **Chemically Controlled Volatile and Nonvolatile Resistive Memory Characteristics of Novel Oxygen-based Polymers**

Brian J. Ree<sup>1,2</sup>, Takuya Isono<sup>2</sup>, and Toshifumi Satoh<sup>2\*</sup>

---

<sup>1</sup>Graduate School of Chemical Sciences and Engineering, Hokkaido University, Sapporo 060-8628, Japan

<sup>2</sup>Faculty of Engineering, Hokkaido University, Sapporo 060-8628, Japan

\*Corresponding author. E-mail: [satoh@eng.hokudai.ac.jp](mailto:satoh@eng.hokudai.ac.jp)

## Abstract

Recent advancements in modern microelectronics continuously increase data storage capacity in modern devices, but it requires delicate and costly fabrication processes. As alternatives to conventional inorganic based semiconductors, semiconducting polymers are of academic and industrial interest for their cost-efficiency, power efficiency, and flexible processability. Here, we have synthesized a series of novel oxygen-based polymers through the post-modification reactions of poly(ethylene-*alt*-maleate) with various oxybenzyl alcohol derivatives. The oxygen-based polymers are thermally stable up to 180°C and their nanoscale film devices exhibit reliable, power efficient *p*-type unipolar volatile and nonvolatile resistive memory characteristics with high ON/OFF current ratios. Additionally, when given a higher number of oxygen atoms in oxyphenyl side chains, the thin film polymer devices demonstrate a wide operational film thickness range. The memory characteristics depend on the oxyphenyl moieties functioning as charge trap sites, where a combination of Schottky emission and trap-limited space charge limited conduction in OFF-state, and hopping conduction in ON-state are observed. This study demonstrates the chemical incorporation of oxyphenyl derivatives into polymer dielectrics as a powerful development tool for *p*-type resistive memory materials.

## 1. Introduction

The advancement of modern microelectronics has marched side by side with the development of data storage devices from the primitive days of punch cards, bulky tape drives to conventional hard disk drives (HDD) and, more recently, compact yet powerful solid state drives (SSD). Conventional HDDs and SSDs are characterized by their large data storage capacity, compact form factors and high data transfer rates. These hallmarks of modern storage devices enable today's individuals to be immersed in a vast array of information with near instantaneous access. The notion of information immersion accompanied by the rapid expansion of information technology infrastructure has opened new

opportunities for our society to acquire new skills and competences necessary for education, training, self-development, employment, and participation in the community.<sup>1</sup> Overall, the 21<sup>st</sup> century could be highlighted as the age of digital information-based society.

This new age of information-based society, ironically, is facing the perpetual growth in the amount of information. Currently, information (i.e., data) gets digitally encoded in binary logical states also known as bits (zeroes and ones), in which eight bits make up a single byte. In 2007, approximately 0.3 zettabytes (1 zettabyte =  $10^{21}$  bytes) of new data were stored worldwide.<sup>2</sup> The 0.3 zettabytes, however, accounts only a portion of all data created in 2007. In 2018, approximately 33 zettabytes of new data were created but, only 15% of the data were stored.<sup>3</sup> In 2025, 175 zettabytes of new data are predicted to be generated with at least a half of the data expected to be stored. This unprecedented growth in amount of data combined with the pressures of deriving value from data for digital transformation will create imperatives for organizations across the whole world over the next decade to develop appropriate data storage, management, and capitalization strategies that bring about a new level of engagement with people using data-informed services and products.<sup>3</sup>

Historically, HDDs have been the most accessible and conventional storage devices but SSDs are slowly becoming the new standard over the recent years due to the much faster data accessibility and smaller form factor. The drawbacks, however, of SSDs reside in the economic and physical aspects. High capacity SSDs are characterized by high number density of transistors in a given integrated circuit chip, which require considerable miniaturization of the transistor's dimension (i.e. feature size). To achieve this, modern lithographic techniques have successfully reduced the feature size of semiconductors inside storage devices from 130 nm in the year 2000 to 10 nm at the present.<sup>4-7</sup> Although this achievement produces high data storage capacity, the mass production of semiconductors with feature size of 10 nm requires lengthy and expensive fabrication processes. Additionally, current lithographic techniques are facing challenges regarding resolution limit and low yield at such small feature size.<sup>5</sup> Moreover, the close distance between the transistors increases the

probability of crosstalks. Furthermore, the densely packed transistors generate a considerable amount of heat requiring additional cooling methods for prolonged use under heavy load. It turns out that the current data storage technologies aiming to follow Moore's law<sup>8</sup> have nearly plateaued in development and are less likely to provide adequate storage capacity of the near future with a sensible cost.<sup>9</sup> Thus, new storage device technologies are urgently in need for storing massive amounts of information with economic efficiency.

For future storage devices, many plausible alternatives have been proposed so far: polymer, molecular, ferroelectric, magnetic, and phase change memories.<sup>4,5,10-13</sup> In particular, polymer memory has gained much attention for its various advantages including easy processability, structural flexibility, miniaturized dimensions, excellent scalability, low-power operation, three-dimensional stacking capability, light weight, wearability, and low-cost potential.<sup>10,14-18</sup> According to chemical structures and constitutions, three different classes of electrical memory polymers have been reported: (i) fully  $\pi$ -conjugated polymers,<sup>10,14-25</sup> (ii) partially  $\pi$ -conjugated polymers with and without additional electroactive units,<sup>10,14-18,26</sup> and (iii) fully non- $\pi$ -conjugated polymers bearing electroactive units.<sup>10,14-18,27-45</sup> The electrical memory characteristics of the fully and partially  $\pi$ -conjugated polymers originate from their affinity to charges. The memory behaviors of the non- $\pi$ -conjugated polymers are known to arise from the innate charge affinities of the incorporated electroactive units. Several chemical groups were reported as suitable electroactive units: carbazole and its derivatives, diphenylamine and their derivatives, triphenylamine and its derivatives, triazole derivatives, pyridine derivatives, fluorene and its derivatives, anthracene and its derivatives, fullerene and its derivatives, oxadiazole and its derivatives, tetracyanoethylene and its derivatives, and tetracyanoquinodimethane.<sup>10,14-18,24-45</sup> Overall, the majority of electrical memory polymers reported in literature are limited to  $\pi$ -conjugated hydrocarbons, nitrogen atom, and their combination. Therefore, the research and development of high performance digital memory polymers are still in

developing stages. The molecular design and synthesis of new memory polymers should be expanded beyond hydrocarbon and nitrogen.

As an expansion of the boundaries of memory polymer development, we report a novel resistive memory polymers based on oxygen containing electroactive units. A series of poly(ethylene-*alt*-maleate)s bearing oxygen constituent and its derivatives as side groups was synthesized: poly(ethylene-*alt*-di(3-methoxybenzyl) maleate) (PEM-BzOMe), poly(ethylene-*alt*-di(3,5-dimethoxybenzyl) maleate) (PEM-BzOMe<sub>2</sub>), poly(ethylene-*alt*-dipiperonyl maleate) (PEM-BzO<sub>2</sub>C), and poly(ethylene-*alt*-di(3,4,5-trimethoxybenzyl) maleate) (PEM-BzOMe<sub>3</sub>) (Figure 1). In addition, poly(ethylene-*alt*-dibenzyl maleate) (PEM-Bz) and poly(ethylene-*alt*-di(4-methylbenzyl) maleate) (PEM-BzMe) were synthesized as reference polymers. All polymers are easily fabricated into nanoscale thin films by conventional spin coating. Synchrotron wide-angle X-ray scattering analysis confirmed that all polymer films are amorphous. The amorphous nanoscale films were determined to reveal electron densities ranging from 373 to 417 nm<sup>-3</sup> (which are equivalent to 1.16–1.32 g cm<sup>-3</sup> in mass density) by synchrotron X-ray reflectivity analysis. The new polymers bearing oxyphenyl-based moieties (i.e., PEM-BzOMe, PEM-BzOMe<sub>2</sub>, PEM-BzO<sub>2</sub>C, and PEM-BzOMe<sub>3</sub>) showed *p*-type unipolar resistive memory behaviors with low switching-ON voltage, high ON/OFF current ratios, long retention time, and various operation thickness windows. In contrast, the reference polymers could exhibit only dielectric characteristics rather than memory behaviors. Considering the chemical nature (chemical composition, inductive effect, resonance effect, and molecular orbitals) and nanoscale film morphology, the polymers are further examined in order to understand their electrical switching mechanisms.

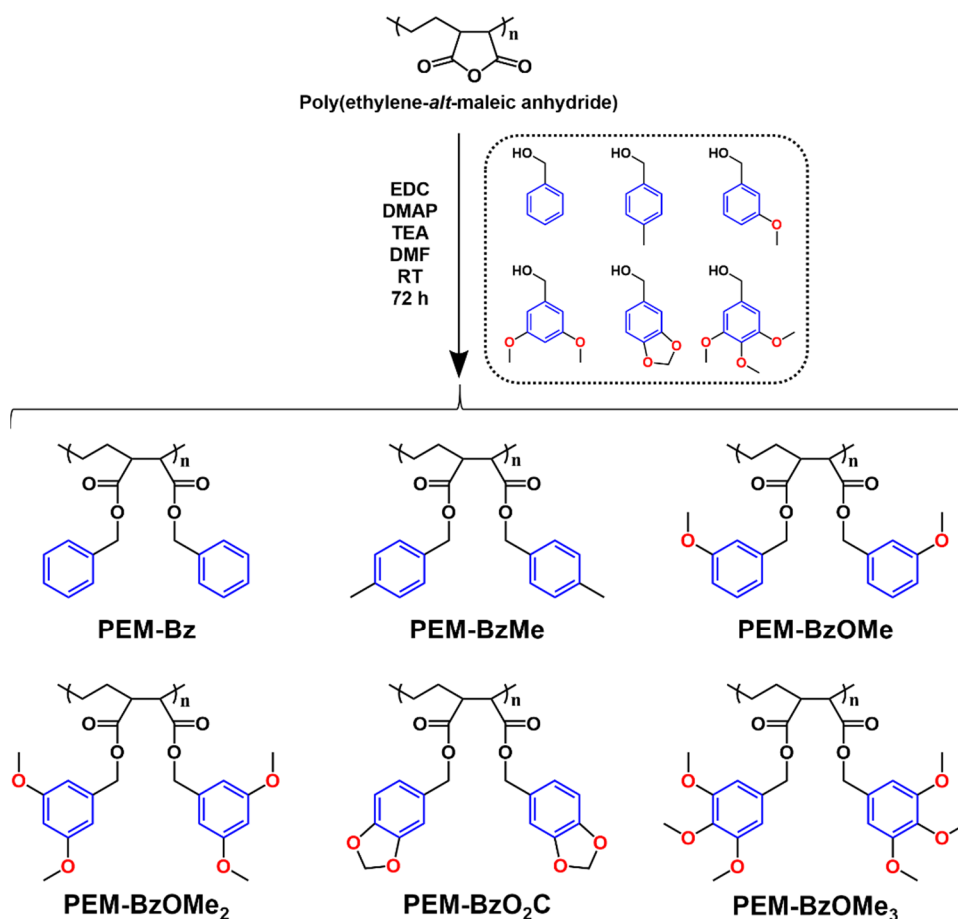


**Figure 1.** Post-modification reaction schemes of poly(ethylene-*alt*-maleic anhydride) (PEM) with various alcohols; EDC: 1-(3-dimethylaminopropyl)-3-ethylcarbodiimide hydrochloride; DMAP: 4-dimethylaminopyridine; TEA: trimethylamine; DMF: dimethylformamide; RT: room temperature.

## 2. Experimental Section

**2.1. Materials.** Poly(ethylene-*alt*-maleic anhydride) (PEM, powder, provided by Sigma-Aldrich;  $M_{n,SEC} = 168.0$  kDa and  $D = 2.85$ , which were measured in this study) was purchased from the Sigma-Aldrich Chemicals Co. (St. Louis, MI, USA) and used as received. 1-(3-Dimethylaminopropyl)-3-ethylcarbodiimide hydrochloride (EDC, >98.0%), 4-dimethylaminopyridine (DMAP, >99.0%), 4-methylbenzyl alcohol (>99.0%), 3-methoxybenzyl alcohol (>97.0%), 3,5-dimethoxybenzyl alcohol (>98.0%), piperonyl alcohol (>98.0%), triethylamine (TEA, >99.0%), and 3,4,5-trimethoxybenzyl alcohol (>98.0%) were purchased from Tokyo Chemical Industry Co., Ltd. (TCI, Tokyo, Japan) and used as received. Benzyl alcohol

(>99.0%) and dry dimethylformamide (DMF; >99.5%; water content, <0.005%) were purchased from Kanto Chemical Co., Inc. (Tokyo, Japan), and used as received.

**2.2. Measurements.** Proton nuclear magnetic resonance ( $^1\text{H}$  NMR) spectra were measured by using JEOL NMR spectrometer (model JNM-ECS400, 400 MHz, JEOL Ltd., Tokyo, Japan). Fourier-transform infrared (FT-IR) spectra were measured with a PerkinElmer Frontier MIR spectrometer (PerkinElmer, Inc., Waltham, MA 02451, USA).

Size exclusion chromatography (SEC) measurements were obtained at 40 °C with JASCO high-performance liquid chromatography system (PU-980 Intelligent HPLC Pump, CO-965 Column Oven, RI-930 Intelligent RI Detector) (JASCO corp., Tokyo, Japan) equipped with a Shodex KD-G 4A guard column (particle size, 8  $\mu\text{m}$ ; 4.6 mm (internal diameter)  $\times$  10 mm (length)), a Shodex Asahipak GF-7M HQ column (linear; particle size, 9  $\mu\text{m}$ ; (7.5 mm  $\times$  300 mm); exclusion limit,  $1 \times 10^7$  (Pullulan)), and a Shodex Asahipak GF-310 HQ column (linear; particle size, 5  $\mu\text{m}$ ; (7.5 mm  $\times$  300 mm); exclusion limit,  $4 \times 10^4$  (Pullulan)) (Showa Denko K. K., Tokyo, Japan). The SEC system was calibrated with poly(methyl methacrylate) (PMMA) standards; dry DMF was used as the eluent.

Thermal stability and phase transitions were examined with a temperature ramping rate of 10.0 °C  $\text{min}^{-1}$  under nitrogen atmosphere by thermogravimetry (TGA; Bruker AXS TG-DTA 2010 SAT, Bruker, Billerica, MA 01821, USA) and differential scanning calorimetry (DSC; TA Instruments DSC Q20, TA Instruments Inc., New Castle, DE 19720, USA).

All synchrotron grazing incidence wide angle X-ray scattering (GIWAXS) measurements were performed at the 3C beamline of the Pohang Accelerator Laboratory (PAL), Pohang, Korea.<sup>43,46-51</sup> Using a X-ray radiation source with a wavelength  $\lambda$  of 0.12301 nm and sample-to-detector distance (SDD) of 210 mm, all scattering data were collected at room temperature in vacuum for 10–30 s with a two-dimensional (2D) charge-coupled detector (CCD) (Rayonix 2D SX 165, Rayonix, Evanston, IL 60201, USA). The incidence angle  $\alpha_i$  of X-ray beam with respect to the film sample surface was set in the range 0.170–0.185°, which is between the critical angle of the polymer film and the silicon

substrate ( $\alpha_{c,f}$  and  $\alpha_{c,s}$ ). Scattering angles were corrected according to the position of the X-ray beam reflected from the silicon substrate as well as by using silver behenate standard (TCI, Tokyo, Japan).

Synchrotron X-ray reflectivity (XR) measurements were conducted in  $\theta$ - $2\theta$  scanning mode at the 3D beamline<sup>43,51-53</sup> of PAL. The X-ray radiation source with  $\lambda = 0.1240$  nm was used and the beam size at the sample position was  $0.1 \text{ mm} \times 2.0 \text{ mm}$ . The collected data were treated with geometrical correction and background subtraction procedures reported in the literature.<sup>43,51,52</sup>

Ultraviolet-visible (UV-vis) spectroscopy measurements were conducted using a Scinco spectrometer (model S-3100, Scinco Co., Ltd., Seoul, Korea). Cyclic voltammetry (CV) measurements were conducted with a scan rate of  $100 \text{ mV s}^{-1}$  in tetrahydrofuran (THF) containing  $0.1 \text{ M } (n\text{C}_4\text{H}_9)_4\text{NClO}_4$  at  $20 \text{ }^\circ\text{C}$  under argon atmosphere using an electrochemical workstation (IM6ex impedance analyzer, ZAHNER-Elektrik GmbH & Co. KG, Kronach, Germany) with three electrodes (a Pt working electrode with a diameter of 1.6 mm, a reference electrode ( $\text{Ag}/\text{Ag}^+/\text{CH}_3\text{CN}/(n\text{C}_4\text{H}_9)_4\text{NClO}_4$ ), and a Pt auxiliary electrode); in the measurements a ferrocene/ferricinium ( $F_c/F_c^+$ ) couple was used as internal standard.

**2.3. Thin Film Preparation.** The individual polymers were dissolved in THF and filtered using disposable syringes equipped with polytetrafluoroethylene filter membranes (pore size,  $0.22 \text{ }\mu\text{m}$ ) to yield polymer solutions with a concentration of 0.5 wt%. Each polymer solution was deposited on silicon (Si) substrates via spin coating process and dried in vacuum at room temperature for 24 h. The film thicknesses were measured to range from 35 to 60 nm through a spectroscopic ellipsometer (Woollam M-2000, J.A. Woollam Co., Lincoln, NE 68508, USA).

**2.4. Polymer Memory Device Fabrication and Test.** The individual polymers were prepared into polymer solutions in THF in concentrations ranging from 0.1 to 5.0 wt% to yield thickness ranging from 10 to 200 nm. All films were deposited on p-doped silicon (d-Si; dopant = boron) substrates via spin coating and dried in vacuum at room temperature for 24 h. Al electrodes (200 nm) were deposited on top of the polymer films by thermal evaporation in vacuum through a

shadow mask to achieve dimensions of  $300 \times 300$ ,  $500 \times 500$ , and  $1000 \times 1000$   $\mu\text{m}$ .  $I - V$  analysis was conducted under ambient air at room temperature, using a semiconductor analyzer (model Keithley 4200, Keithley Instruments, Cleveland, OH 44139, USA).

### 3. Results and Discussions

**3.1. Synthesis of oxyphenyl-based polymers.** To prepare new oxyphenyl-based polymers, a poly(ethylene-*alt*-maleic anhydride) (PEM:  $M_{n,SEC} = 168.0$  kDa and  $D = 2.85$  (dispersity)) was chosen for post-modification reactions to incorporate various oxyphenyl-based moieties. For the modification reactions, four different alcohols were selected as model oxyphenyl-based moiety compounds (4-methoxybenzyl alcohol, 3,5-dimethoxybenzyl alcohol, piperonyl alcohol, and 3,4,5-trimethoxybenzyl alcohol) and two non-oxyphenyl based alcohols (benzyl alcohol, and 4-methylbenzyl alcohol) were chosen to serve as controls (Figure 1). With each alcohol compound, the ring-opening and diesterification reactions of maleic anhydride units in the PEM were attempted to achieve the highest possible conversion. As a result, such reactions were successfully undergone with the aids of 1-(3-dimethylaminopropyl)-3-ethylcarbodiimide hydrochloride (EDC), 4-dimethylaminopyridine (DMAP), and triethylamine (TEA) in dry dimethylformamide (DMF) at room temperature for 72 h; synthesis details are in Supporting Information. The obtained products were characterized by Fourier transform infrared (FTIR) and proton nuclear magnetic resonance ( $^1\text{H}$  NMR) spectroscopies. PEM revealed a clear carbonyl symmetric stretching peak around  $1850\text{ cm}^{-1}$  and a carbonyl asymmetric stretching peak around  $1770\text{ cm}^{-1}$  of the maleic anhydride units in the FTIR spectrum (Figure S1a). The carbonyl asymmetric stretching peaks were no longer discernible in the spectra of the target products; instead, an ester carbonyl stretching peak around  $1730\text{ cm}^{-1}$  were observed (Figures S1b-g). Additionally, the products bearing methoxy groups exhibited enhanced C-H stretching peaks at  $2700\text{--}3050\text{ cm}^{-1}$ . The  $^1\text{H}$  NMR spectroscopy analyses also confirmed characteristic chemical shifts of the backbone unit and the incorporated oxyphenyl-based moieties

(Figures S2-S7). The increase in molecular weight due to the incorporated oxyphenyl-based moieties were further determined by size exclusion chromatography (SEC) analysis (Figure S8; Table 1). These characterization results collectively indicate that the incorporations of the oxyphenyl-based moieties into the PEM polymers were successfully performed via the ring-opening and diesterification reactions of maleic anhydride units. The conversion of each reaction could be determined from the integrals of characteristic chemical shifts (i.e., the protons of the backbone and the incorporated moieties) in the  $^1\text{H}$  NMR spectra (Figures S2-S7). The obtained reaction conversions range from 89 to 94 % (Table 1). Overall, the reaction conversions are slightly lower than 100 %, which could be caused by steric hindrance due to the higher density of maleic anhydride units in the backbone.

**3.2. Thermal characterization.** The modified polymers have been determined to be thermally stable up to 180 °C or higher temperatures ( $= T_{d,5}$ , temperature at which 5.0 wt% weight loss takes place) depending on the incorporated moieties by thermogravimetry (TGA) analysis (Table 1; Figure S9). PEM-BzOMe<sub>3</sub> exhibits the highest  $T_{d,5}$  (200 °C), whereas PEM-BzMe shows the lowest  $T_{d,5}$  (180 °C). The other polymers reveal  $T_{d,5}$  values between those of PEM-BzMe and PEM-BzOMe<sub>3</sub>. These  $T_{d,5}$  values are relatively lower than that (302 °C) of PEM (Table 1; Figure S10).

The polymers were further subjected to differential scanning calorimetry (DSC) analysis. PEM-BzOMe reveals a glass transition at 10 °C ( $= T_{g,\text{onset}}$ , onset temperature of glass transition), whereas PEM-BzOMe<sub>3</sub> exhibits  $T_{g,\text{onset}} = 45$  °C (Table 1; Figure S11). The other polymers show glass transition temperatures between those of PEM-BzOMe and PEM-BzOMe<sub>3</sub>. All  $T_{g,\text{onset}}$  values are lower than that (136 °C) of PEM (Table 1; Figure S12). All polymers and their base polymer only exhibit glass transitions; no crystal melting transitions could be observed. These results collectively indicate that all modified polymers and their base polymer are amorphous.

**Table 1. Characteristics of the polymers prepared in this study**

Polymer	$M_{n,SEC}^a$ (kDa)	$D^b$	Conversion $^c$ (%)	$T_{g,onset}^d$ (°C)	$T_{d,5}^e$ (°C)
PEM-Bz	168.0	2.85	94	26	186
PEM-BzMe	307.0	3.23	93	30	180
PEM-BzOMe	233.0	4.80	92	10	192
PEM-BzOMe <sub>2</sub>	312.5	4.34	91	27	199
PEM-BzO <sub>2</sub> C	334.0	3.77	90	42	194
PEM-BzOMe <sub>3</sub>	312.0	4.29	89	45	200
PEM	167.5	2.85		136	302

<sup>a</sup>Number-averaged molecular weight measured by SEC with PMMA standards; DMF containing 0.01 M LiCl was used as the eluent. <sup>b</sup>Dispersity measured by SEC analysis with PMMA standards. <sup>c</sup>The conversion of esterification reaction which was determined by <sup>1</sup>H NMR spectroscopy analysis. <sup>d</sup>Onset temperature of glass transition at a heating rate of 10 °C/min in differential scanning calorimetry (DSC) in a nitrogen atmosphere. <sup>e</sup>Temperature at which 5.0 wt% weight loss occurred in nitrogen atmosphere; a heating rate of 10 °C/min was employed.

**3.3. Synchrotron X-ray reflectivity.** All polymers were found to be soluble in common organic solvents such as DMF, tetrahydrofuran (THF), and dichloromethane (CH<sub>2</sub>Cl<sub>2</sub>). They were processed as nanoscale films on silicon substrates via conventional spin coating and subsequent drying process in vacuum at room temperature for 24 h to yield film thickness ranging from 35 to 61 nm. The obtained nanoscale films were examined by synchrotron X-ray reflectivity (XR) analysis (Figure 2). The XR data could be satisfactorily fitted by the Parratt algorithm.<sup>54,55</sup> The XR analysis confirms that PEM-BzMe exhibits the lowest electron density  $\rho_e$  (373 electrons nm<sup>-3</sup>) while both PEM-BzOMe and PEM-BzO<sub>2</sub>C reveal the highest  $\rho_e$  (417 electrons nm<sup>-3</sup>) (Table 2). Furthermore, this XR analysis found that the polymer films exhibit surface roughness ranging from 0.42 to 0.95 nm. With respect to the overall film thickness, the surface roughness values indicate that the polymer films are capable of forming good quality thin films via conventional solution cast and subsequent drying process.

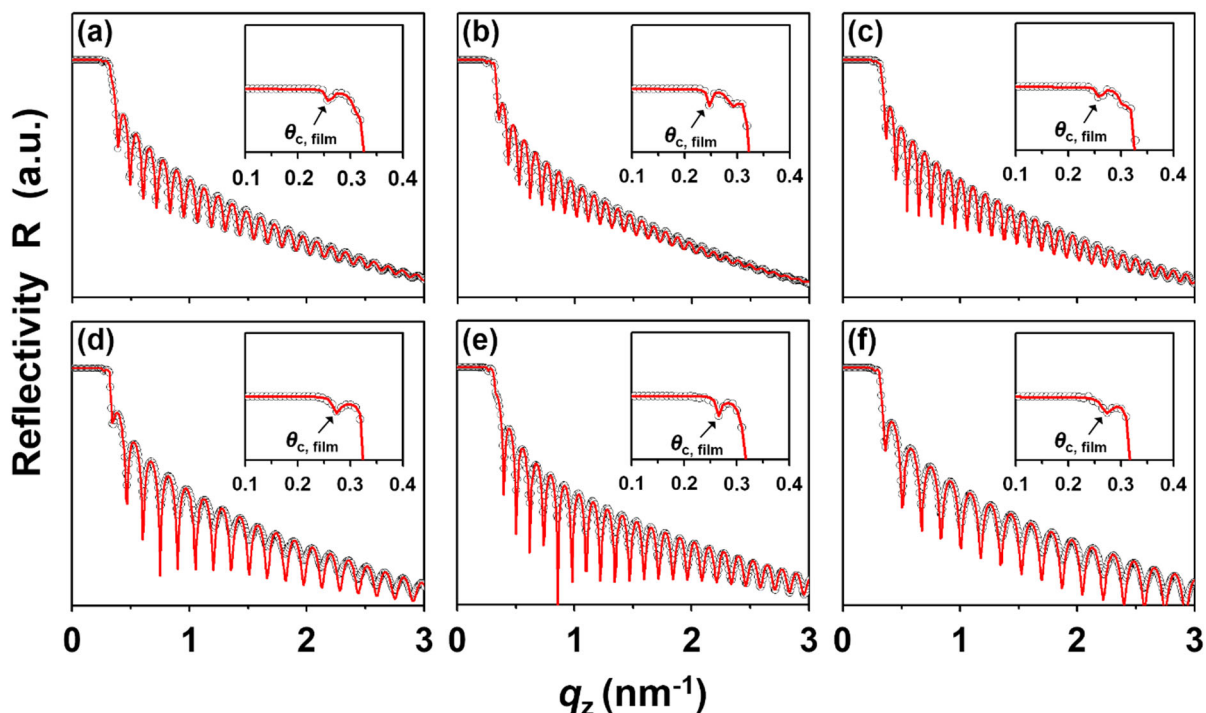


**Figure 2.** Representative XR profiles of nanoscale films of the polymers synthesized in this study: (a) PEM-Bz; (b) PEM-BzMe; (c) PEM-BzOMe; (d) PEM-BzOMe<sub>2</sub>; (e) PEM-BzO<sub>2</sub>C; (f) PEM-BzOMe<sub>3</sub>. The open circles represent the measured data; the red lines were obtained by fitting the data using the Parratt algorithm. An X-ray source of  $\lambda = 0.1240$  nm was used.

**3.4. Synchrotron grazing incidence wide angle X-ray scattering.** The nanoscale polymer films were further characterized by synchrotron grazing incidence wide angle X-ray scattering (GIWAXS). The films show one to three scattering halos, depending on the polymers (Figures 3 and S13). The lack of specific scattering spots or peaks in conjunction with the presence of scattering halos indicate that all polymers of this study are amorphous rather than crystalline or semi-crystalline. PEM-BzOMe<sub>3</sub> reveals three isotropic halos at 4.7, 12.7, and 16.8° (Figures 3 and S13f). Taking into consideration its amorphous nature and chemical structure, the first halo (4.7°) could be assigned to the mean interdistance of polymer chains, the second halo (12.7°) could be assigned to the mean interdistance between the polymer backbone and the side group, and the third halo (16.8°) could be assigned to the mean interdistance of side groups. The isotropic nature further informs that the polymer chains are randomly oriented inside the nanoscale film. In comparison,

PEM-Bz and PEM-BzMe apparently show two anisotropic halos (Figures 3 and S13a-b). The scattering intensities of the two halos are relatively stronger along the out-of-plane direction, indicating that the polymer chains exhibit orientational bias towards the horizontal direction (i.e. in-plane of the substrate). Furthermore, their second halo is relatively broader and centered at an angle between those of the second and third halos of PEM-BzOMe<sub>3</sub>. These facts suggest that the halo, which originates from the mean interdistance between the polymer backbone and the side group, is heavily overlapped with one for the mean interdistance of side groups. This kind of heavy overlap is also observed in the scattering patterns of PEM-BzOMe, PEM-BzOMe<sub>2</sub>, and PEM-BzO<sub>2</sub>C (Figures 3 and S13c-e). Such overlap is relatively lower for PEM-BzO<sub>2</sub>C; hence, the overlapped rings appear much broader. These halos are, however, isotropic, indicating that polymer chains are randomly oriented in the films. For all halos, *d*-spacing values have been estimated and compared in Table 2. The *d*-spacing ranges in 1.050–1.530 nm for the first halo, 0.442–0.525 nm for the second halo, and 0.368–0.411 nm for the third halo.

**Table 2.** Structural parameters and densities of the polymer films prepared in this study

Polymer film	First peak <sup>a</sup>		Second peak <sup>b</sup>		Third peak <sup>c</sup>		Thickness <sup>f</sup> (nm)	$\rho_e^g$ (nm <sup>-3</sup> )	$\rho_g^h$ (g cm <sup>-3</sup> )
	$d_{1,\perp}^d$ (nm)	$d_{1,\parallel}^e$ (nm)	$d_{2,\perp}^d$ (nm)	$d_{2,\parallel}^e$ (nm)	$d_{3,\perp}^d$ (nm)	$d_{3,\parallel}^e$ (nm)			
PEM-Bz	1.050 (5.98°) <sup>i</sup>	1.050 (5.42°)	0.455 (14.82°)	0.445 (14.72°)	- <sup>j</sup>	-	51.5 (0.7) <sup>k</sup>	401	1.26
PEM-BzMe	1.190 (5.16°)	1.180 (4.75°)	0.445 (14.55°)	0.442 (14.49°)	-	-	60.7 (0.9)	373	1.16
PEM-BzOMe	1.100 (5.46°)	1.080 (5.11°)	-	-	0.400 (15.39°)	0.393 (15.16°)	58.2 (0.7)	417	1.31
PEM-BzOMe <sub>2</sub>	1.200 (4.77°)	1.350 (4.65°)	-	-	0.368 (16.41°)	0.408 (16.23°)	40.2 (0.5)	412	1.29
PEM-BzO <sub>2</sub> C	1.000 (6.12°)	-	0.471 (14.94°)	0.480 (14.39°)	0.411 (17.44°)	0.395 (16.89°)	50.2 (0.5)	417	1.32
PEM-BzOMe <sub>3</sub>	1.200 (4.78°)	1.530 (4.59°)	0.525 (12.98°)	0.510 (12.53°)	0.395 (16.93°)	0.380 (16.79°)	35.6 (0.4)	392	1.23

<sup>a</sup>The scattering peak positioned around 5°. <sup>b</sup>The scattering peak positioned in the range of 10–20°. <sup>c</sup>The scattering peak positioned in the range of 10–20°. <sup>d</sup>The *d*-spacing of the scattering peak along the  $\alpha_f$  direction (i.e., out-of-plane direction). <sup>e</sup>The *d*-spacing of the scattering peak along the  $2\theta_f$  direction (i.e., in-plane direction). <sup>f</sup>Film thickness

determined by synchrotron XR analysis. <sup>g</sup>Average electron density determined by XR analysis. <sup>h</sup>Mass density obtained from the electron density and chemical composition. <sup>i</sup>The angle of scattering peak. <sup>j</sup>Could not be distinguishable due to either heavy overlap or too weak. <sup>k</sup>Surface roughness.

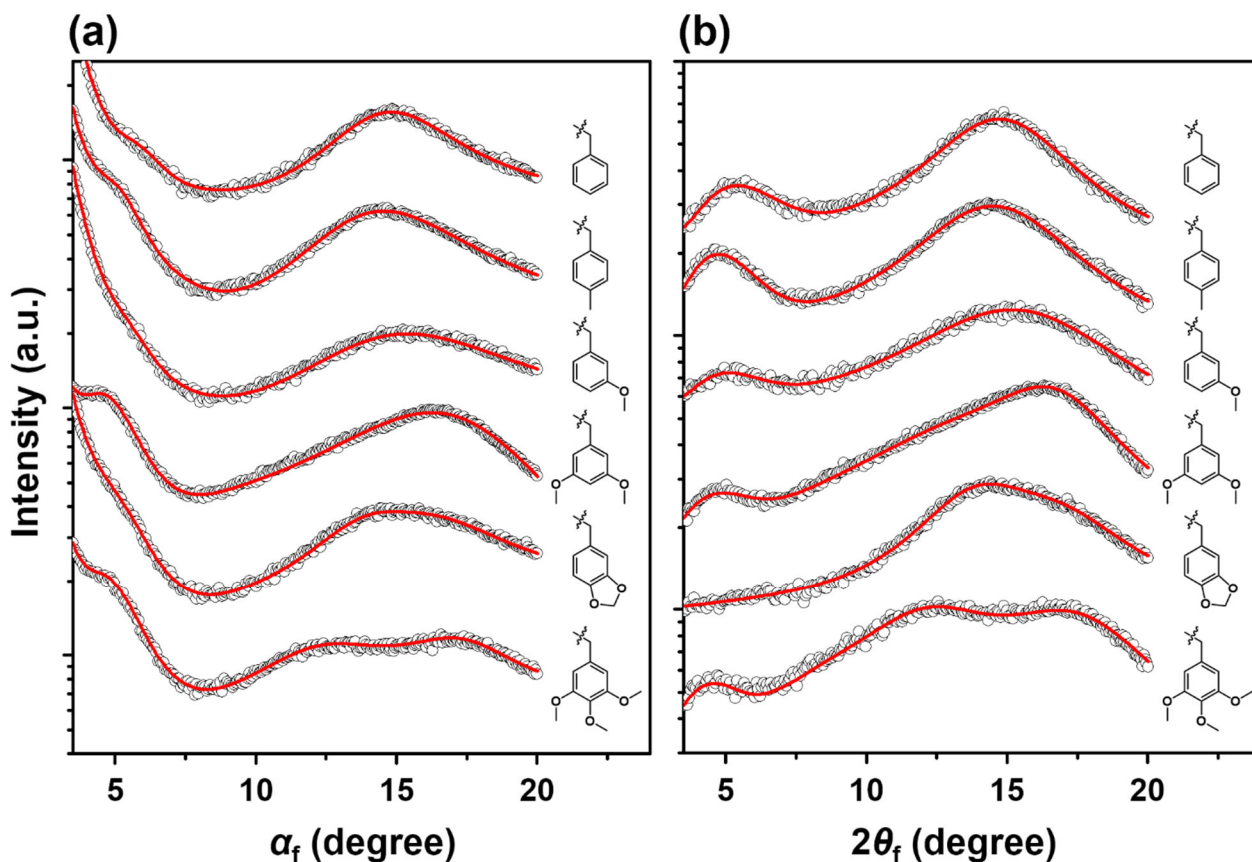


**Figure 3.** Representative 1D scattering profiles of nanoscale films (35–61 nm thick) of the polymers extracted from synchrotron 2D GIXS images (Figure S13) measured with an X-ray source of  $\lambda = 0.1230$  nm at a sample-to-detector distance (SDD) of 210 mm. (a) 1D profiles extracted along the  $\alpha_f$  direction (i.e., vertical direction) at  $2\theta_f = 0.011^\circ$ ; (h) 1D profiles extracted along the  $2\theta_f$  direction (i.e., horizontal direction) at  $\alpha_f = 0.388^\circ$  (PEM-Bz) or  $0.377^\circ$  (the other polymers). The open circles represent the measured scattering intensity; the red lines are the calculated intensity from the fitted results.

**3.5. Molecular orbital characterization.** For the polymers, cyclic voltammetry (CV) and ultraviolet-visible (UV-vis) spectroscopy analyses were performed to characterize molecular orbitals (highest occupied molecular orbital (HOMO) and lowest molecular orbital (LUMO)) and band gaps. The HOMO energy ( $E_{\text{HOMO}}$ ) levels of all polymers were obtained from the measured oxidation half-wave potentials ( $E_{1/2}$ ) vs Ag/AgCl (Fig S14), under the assumption that the  $E_{\text{HOMO}}$  of the  $F_c/F_{c+}$  standard is  $-4.80$  eV with respect to the zero vacuum level. The band gaps ( $E_{\text{bg}}$ ) of the polymers were

measured by UV-vis spectroscopy analysis (Fig S15). From the  $E_{\text{HOMO}}$  and  $E_{\text{bg}}$  data, the LUMO energy ( $E_{\text{LUMO}}$ ) levels were calculated. Overall, depending on the incorporated side groups,  $E_{\text{HOMO}}$  ranges between  $-4.61$  and  $-4.72$  eV, whereas  $E_{\text{LUMO}}$  varies from  $-1.38$  to  $-2.25$  eV;  $E_{\text{bg}}$  is in a range of  $2.43$  to  $3.99$  eV (Table 3).

**Table 3.** Molecular orbitals, band gaps, and energy barriers of the polymers prepared in this study

Polymer	$E_{\text{HOMO}}^a$ (eV)	$E_{\text{LUMO}}^b$ (eV)	$E_{\text{bg}}^c$ (eV)	$ E_{\text{HOMO}} - \Phi ^d$ (eV)	$ E_{\text{LUMO}} - \Phi ^e$ (eV)
PEM-Bz	-4.62	-1.38	3.24	0.34 <sup>f</sup> / 0.18 <sup>g</sup>	2.90 <sup>h</sup> / 3.42 <sup>i</sup>
PEM-BzMe	-4.68	-0.69	3.99	0.40 / 0.12	3.59 / 4.11
PEM-BzOMe	-4.68	-2.25	2.43	0.40 / 0.12	2.03 / 2.55
PEM-BzOMe <sub>2</sub>	-4.62	-2.18	2.44	0.33 / 0.17	2.48 / 3.00
PEM-BzO <sub>2</sub> C	-4.61	-2.16	2.45	0.33 / 0.17	2.12 / 2.64
PEM-BzOMe <sub>3</sub>	-4.72	-2.24	2.48	0.44 / 0.08	2.04 / 2.56

<sup>a</sup>Highest occupied molecular orbital level. <sup>b</sup>Lowest unoccupied molecular orbital level. <sup>c</sup>Band gap. <sup>d</sup>The energy barrier of HOMO level to the work function  $\Phi$  of an electrode. <sup>e</sup>The energy barrier of LUMO level to the work function  $\Phi$  of an electrode. <sup>f</sup>The energy barrier of HOMO level to the work function  $\Phi$  ( $= -4.28$  eV) of aluminum electrode. <sup>g</sup>The energy barrier of HOMO level to the work function  $\Phi$  ( $= -4.80$  eV) of highly boron-doped silicon electrode. <sup>h</sup>The energy barrier of LUMO level to the work function of aluminum electrode. <sup>i</sup>The energy barrier of LUMO level to the work function of highly boron-doped silicon electrode.

**3.6. Resistive memory characterization.** With the polymers, thin film resistive memory devices were fabricated in an electrode/polymer/electrode structure using *p*-doped silicon substrate (d-Si; dopant = boron) as a bottom electrode and aluminum layer as a top electrode (Figures 4a-b). Both PEM-Bz and PEM-BzMe exhibit dielectric behaviors in positive and negative voltage sweeps and their reverse sweeps, even though their films are very thin (ca. 10 nm) (Figures 4c-d).

Surprisingly PEM-BzOMe, however, reveals electrical switching behaviors (Figure 4e). The 11.3 nm thick film is initially in an OFF-state at 0 V. When positive bias is applied, the electrical current  $I$  steadily increases with applying voltage  $V$  until 3.0 V where a sudden transition to a higher current level is observed ( $= V_{\text{c,ON}}$ , critical switching-ON voltage). The high current level is maintained until the maximum applied voltage of 7.0 V. In the subsequent reverse sweep (7.0 V  $\rightarrow$  0 V), such high current level is retained until ca. 2.0 V. With further decreasing voltage, the current level decreases

and eventually returns to the OFF-state when electrical power is turned off. Similar electrical switching-ON and OFF behaviors are observed in the negative voltage sweep. Similar switching behaviors are further discernible in film thicknesses of 18.7 and 31.1 nm (Figure S16). At 50.2 nm, however, this polymer exhibits dielectric characteristics. Collectively, PEM-BzOMe successfully demonstrates excellent unipolar dynamic random access memory (DRAM, a volatile memory) behaviors over a limited thickness range of <50 nm. Even within such thickness limit,  $V_{c,ON}$  is increased with increasing film thickness (Figure S20a). A similar trend of DRAM behaviors is observed for PEM-BzOMe<sub>2</sub> in the thickness range of <30 nm (Figures 4f, S17, and S20b).

Interestingly, quite different switching behaviors are observed for PEM-BzO<sub>2</sub>C. In the case of 10.3 nm devices, switching-ON takes place in both positive and negative voltage sweeps;  $V_{c,ON}$  is 3.8 V in the positive voltage sweep and -4.2 V in the negative sweep (Figures 4g-h). However, once switched on, the films could not be returned to the OFF-state in the subsequent reverse voltage sweeps as well as in the subsequent opposite voltage sweeps. Moreover, the ON states are retained even after electrical power is turned off. Overall, the 10.3 nm device demonstrates a permanent, non-volatile memory characteristic in the form of unipolar write-once-read-many-times (WORM) memory. WORM memory behaviors are further discernible in 17.7 nm devices (Figure S18a).

At 38.0 nm of polymer film thickness, however, the observed memory behavior changes to DRAM memory mode; such DRAM memory behaviors are observed for devices with film thickness less than <136 nm (Figures S18b-f and S20c). A very similar trend of digital memory behaviors is observed for PEM-BzOMe<sub>3</sub>, with the exception of DRAM behavior persisting to a higher film thickness of 165 nm and dielectric behavior observed at a film thickness of 209 nm (Figures 4i-j, S19, and S20d).

The devices revealing digital memory behaviors were additionally tested from the aspect of reliability (Figure 5). The PEM-BzOMe (11.3 nm) device maintains the OFF-state as well as the ON-state for 40,000 s in air ambient condition. Similar level of reliability is confirmed for the PEM-BzOMe<sub>2</sub> (11.1 nm) device in air ambient condition. The PEM-BzO<sub>2</sub>C (10.3 nm) and PEM-BzOMe<sub>3</sub>

(12.2 nm) devices show highly stable OFF-state and ON-state in air ambient condition as permanent memory devices. Similar stabilities were observed for the other memory devices.

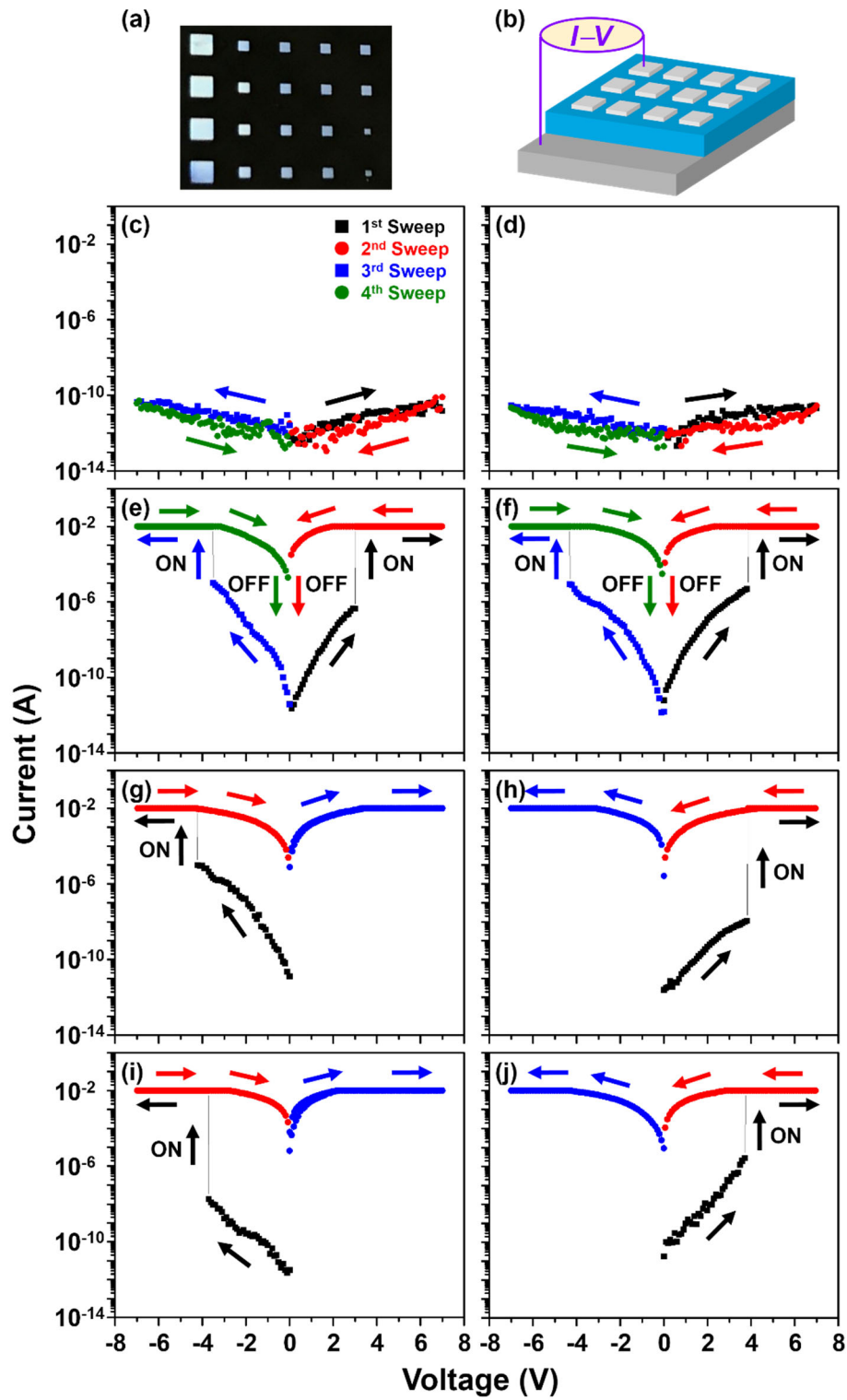


**Figure 4.** Representative  $I$ - $V$  curves of the boron-doped silicon(d-Si)/polymer/Al devices, which were measured with a compliance current set of 0.01 A in air ambient condition: (a) fabricated device cells; (b) schematic device

cells and  $I$ - $V$  measurement; (c) PEM-Bz (9.7 nm thick); (d) PEM-BzMe (12.0 nm); (e) PEM-BzOMe (11.3 nm); (f) PEM-BzOMe<sub>2</sub> (11.1 nm); (g, h) PEM-BzO<sub>2</sub>C (10.3 nm); (i, j) PEM-BzOMe<sub>3</sub> (12.2 nm). The electrode contact area was  $500 \times 500 \mu\text{m}^2$ .

As described above, all digital memory devices are confirmed to stably function even in air ambient condition. They show high ON/OFF current ratios ranged from  $1.0 \times 10^3$  to  $1.0 \times 10^8$ , depending on the reading voltages and the incorporated oxygen-containing moieties. Their switching-ON voltages are lower than  $\pm 7$  V, depending on the type of incorporated oxygen-containing moieties. Moreover, the resistive memory type could be controlled between volatile or non-volatile through the selection of oxygen-containing moiety and adjusting film thickness. Overall, they demonstrate excellent levels of unipolar resistive memory performance.

These interesting memory behaviors may stand on the chemical, physical, electrical, and morphological natures of the polymers. In particular, it is quite intriguing to comprehend which factors and mechanisms are functioning as the driving force behind such high performing memory characteristics. Therefore, we try to consider the chemical structure, the molecular orbital energy levels, the charge-oxyphenyl moiety interaction, charge affinity, and resonance effect associated with the novel polymers to discuss the memory behaviors in detail as follows.

This study confirmed that PEM-Bz and PEM-BzMe are dielectric. Given that the starting material PEM is a known dielectric material, it can be concluded that the hydrocarbon-based vinyl backbone as well as the ester linkers, the benzyl moieties and the methylbenzyl moieties as side groups do not contribute to induce resistive memory behaviors. In contrast, PEM-BzOMe, PEM-BzOMe<sub>2</sub>, PEM-BzO<sub>2</sub>C and PEM-BzOMe<sub>3</sub> exhibit both non-volatile and volatile memory characteristics. Comparing the chemical structures of the polymers informs that, despite having the same vinyl backbone and the ester linkers as PEM-Bz and PEM-BzMe, the presence of oxygen atoms adjacent to phenyl units as the forms of monomethoxy, dimethoxy, trimethoxy and methylenedioxy substituents is the driving force behind the memory characteristic. In other words, the local distribution of the monomethoxyphenyl, dimethoxyphenyl, trimethoxyphenyl and methylenedioxyphenyl moieties throughout the dielectric matrix formed by the vinyl backbone and

the ester linkages is correlated to the semiconducting nature of PEM-BzOMe, PEM-BzOMe<sub>2</sub>, PEM-BzO<sub>2</sub>C and PEM-BzOMe<sub>3</sub>.

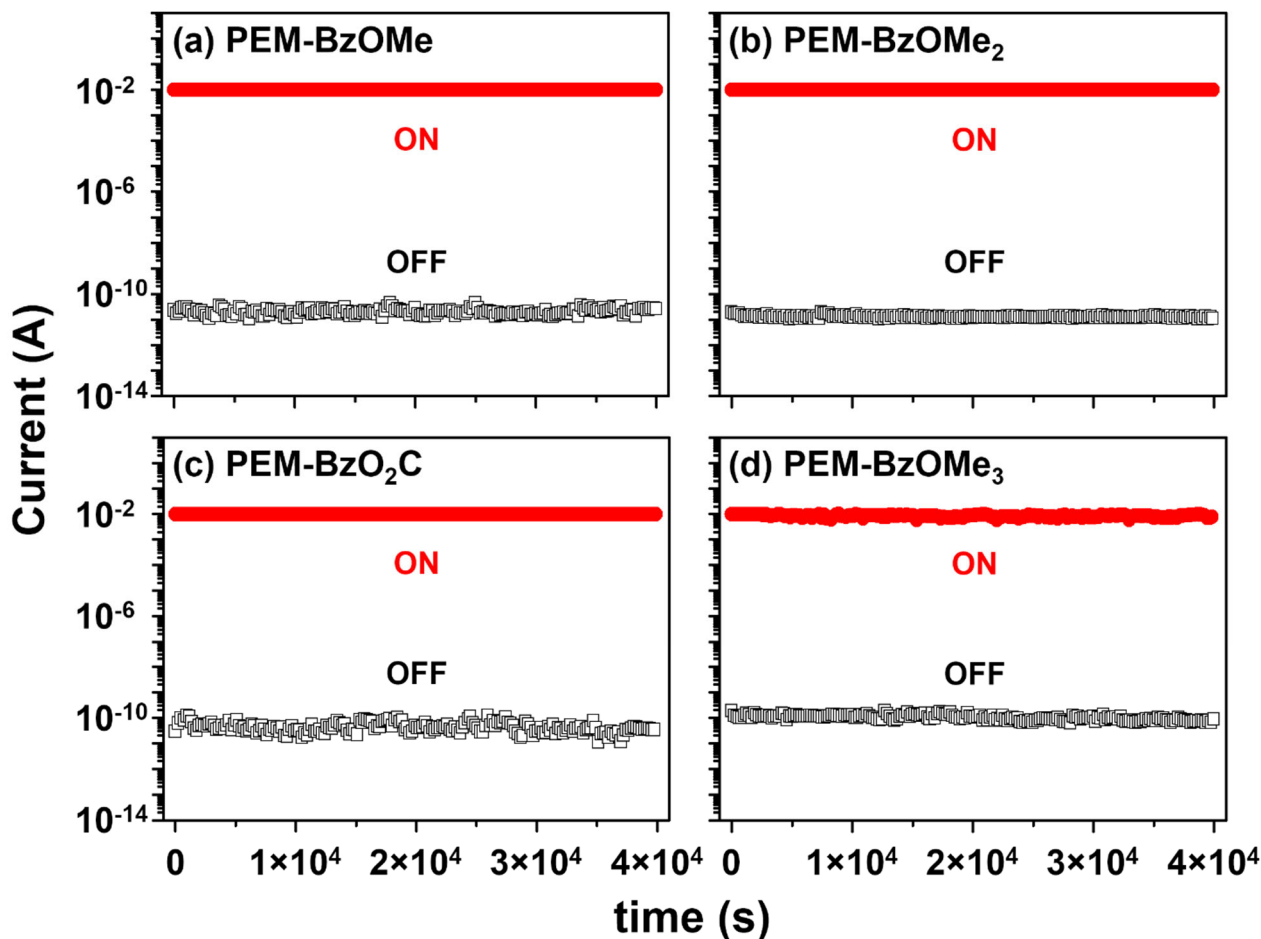


**Figure 5.** Representatives of the retention times of d-Si/polymer/Al devices in ON- and OFF-states, which were measured with a compliance current of 0.01 A in air ambient condition: (a) PEM-BzOMe (11.3 nm thick); (b) PEM-BzOMe<sub>2</sub> (11.1 nm); (c) PEM-BzO<sub>2</sub>C (10.3 nm); (d) PEM-BzOMe<sub>3</sub> (12.2 nm). The reading voltage was 1.0 V for the OFF-state and 5.0 V for the ON-state. The electrode contact area was 500 × 500 μm<sup>2</sup>.

Molecular orbital energy level analysis provides further insight regarding the nature of the semiconducting phenomenon for the polymers. Table 3 shows that the magnitude of  $|E_{\text{HOMO}} - \Phi|$  values are six to thirty-four times smaller than the  $|E_{\text{LUMO}} - \Phi|$  values for all the polymers of this study. Smaller  $|E_{\text{HOMO}} - \Phi|$  values indicate that all polymers are likely to have hole injections into the HOMO level from the electrodes rather than the electron injections into the LUMO level. As a result, PEM-BzOMe, PEM-BzOMe<sub>2</sub>, PEM-BzO<sub>2</sub>C and PEM-BzOMe<sub>3</sub> can be classified as *p*-type memory materials where the current running through the polymer films is dominated by holes.

The interaction between the oxyphenyl moieties and injected holes in the OFF- and ON-states can be described in detail based on the analysis of the  $I-V$  profiles. In the OFF-state, the four memory polymers present three-regime behaviors in the  $I-V$  profiles (Figure 6a, S21a, S22a and S23a). The  $I-V$  data in the first-regime (i.e., *regime-I*) could be successfully fitted by using a Schottky emission conduction model,<sup>56-58</sup> whereas those in the second- and third-regimes (*regime-II* and III) could be well fitted with trap-limited space charge limited conduction (SCLC) model.<sup>59,60</sup> They further show single regime behaviors in the  $I-V$  data of ON-state (Figure 6b, S21b, S22b and S23b). The  $I-V$  data of ON-state could be well fitted by using either a hopping conduction model<sup>61,62</sup> or an Ohmic conduction model.<sup>63</sup> Here, it is noted that the PEM-Bz and PEM-BzMe dielectrics always reveal  $I-V$  profiles that follow *regime-I* trend that exhibits Schottky emission conduction model (Figure S24). This may be a clue about why they could not exhibit any memory behaviors. Collectively, the analysis results inform that the *p*-type volatile and/or non-volatile memory behaviors could be governed by Schottky emission conduction combined with trap-limited SCLC mechanism in the OFF-state. In the ON-state, hopping conduction mechanism utilizes the locally-distributed electroactive oxyphenyl moieties as charge trap sites and charge hopping sites for current flow. A detailed description of the theorized conduction mechanism and proposed schematic (Figures 6c, S21c, S22c and S23c) is as follows. In *regime-I*, holes are injected into the polymer-electrode interface from the aluminum electrode until the applied electric potential reaches a critical transitional voltage  $V_{tr}$ , in which the holes transition from stationary injected state to transporting state. In *regime-II*, the injected holes are transported to and trapped in the electroactive sites within the polymer film by exhibiting behaviors of space charge. Such charge trapping process continues until a critical point of charge trap saturation voltage  $V_{CTS}$ . In *regime-III*, all electroactive sites are saturated, and an excess of holes continually injected from the polymer-electrode interface begin to build up and actively traverse inside the polymer layer while retaining characteristics of space charges. When the electric potential reaches the critical switching-ON voltage  $V_{c,ON}$ , the excess of injected holes flow through the whole polymer layer from the aluminum electrode to the doped silicon substrate via hopping process using the charged trapped sites as stepping stones.

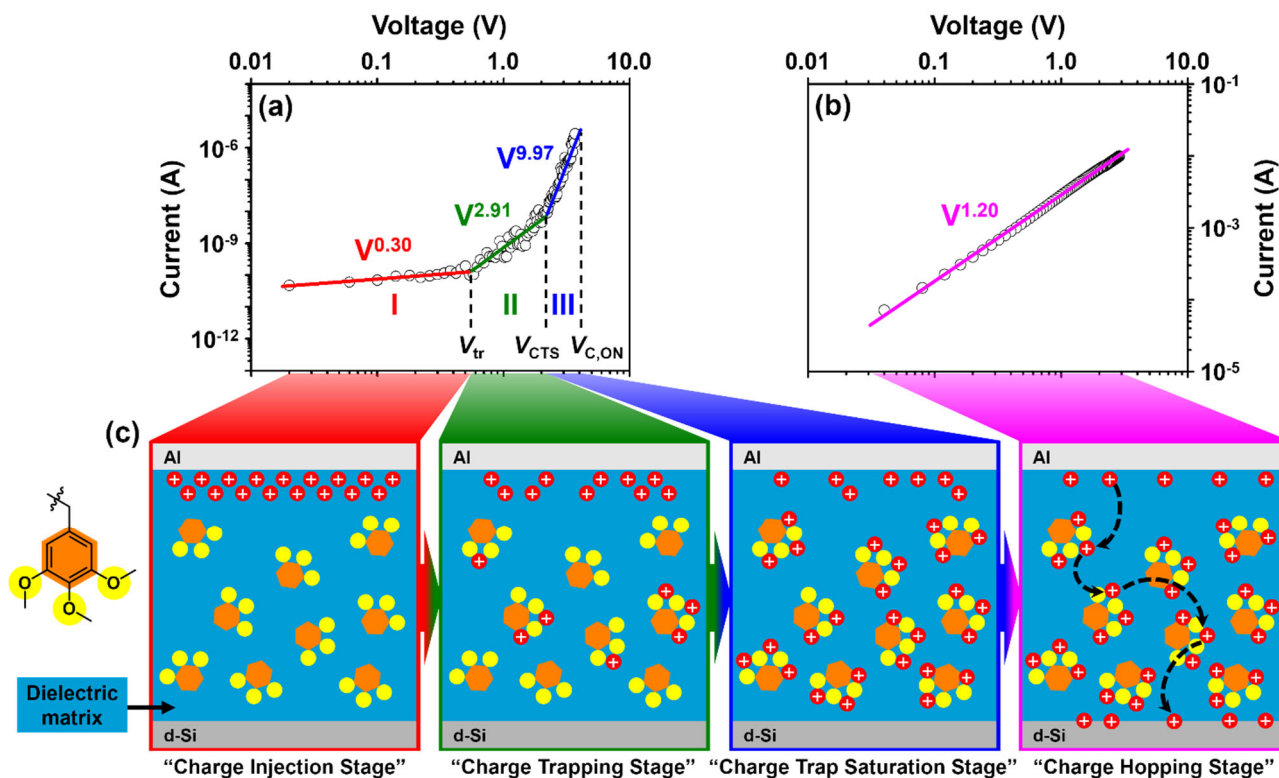


**Figure 6.**  $I$ - $V$  data analysis of the d-Si/PEM-BzOMe<sub>3</sub>(12.2 nm thick)/Al devices which were measured with a compliance current of 0.01 A in air ambient condition: (a) OFF-state where the symbols are the measured data and the solid lines represent the fit results using Schottky emission conduction and trap-limited SCLC models; (b) ON-state where the symbols are the measured data and the solid line represents the fit results using hopping conduction model; (c) schematic diagrams of charge injection, trap, trap-saturation, and hopping process (i.e., transportation) between two electrodes via using oxyphenyl-based moieties (trimethoxybenzyl: BzOMe<sub>3</sub>) as electroactive sites.  $V_{tr}$  is the voltage starting to transfer charges from the charge injection stage to the charge trapping stage;  $V_{CTS}$  denotes the on-set voltage reaching to the charge trap saturation stage from the charge trapping stage;  $V_{c,ON}$  denotes the switching-ON voltage.

Regarding the charge trapping and hopping processes utilizing the locally-distributed electroactive moieties, one may expect higher molecular packing and higher density to benefit and improve the memory performance. However, it is difficult to rationalize such correlation of morphological and physical properties to the memory performance from the results of this study. For example, PEM-BzOMe shows a very limited memory performance in comparison to PEM-BzOMe<sub>3</sub>, despite exhibiting a higher electron density as well as a relatively shorter interchain distance than PEM-BzOMe<sub>3</sub>. Therefore, the molecular packing and density characteristics (Table 2) do not have correlations to the charge trapping and hopping processes, and the observed memory characteristics.

All polymers of this study are chemically analogues each other, which are based on polyvinyl backbone and benzyl ester side groups; they have only different substituents on the phenyl unit in the side group (Figure 1). Nevertheless, they exhibit significantly different electric behaviors as discussed above. Thus, one can raise the following question: Why could they reveal such different electrical characteristics? Two factors are considered to play critical roles on the electrical behaviors as follows. The first considerable factor is the affinity for charges (holes and/or electrons). The polyvinyl backbone may have relatively quite low affinity for charges because of low electronegativities of the carbon and hydrogen atomic components and the covalent bonding amongst them. The ester linker is composed of a carbonyl unit having a certain level of polarity and an ether oxygen atom having two lone pair electrons; thus, the ester linkers may have some affinity for charges. Phenyl group is known as a weak electron acceptor and hence has an affinity to charges although the level is relatively low. Methyl and methylene units are known as weak electron donors because of their nonpolarities and covalent bonding characters. Methoxy and methylenedioxy units are known as good electron donors and their oxygen atoms have two lone pair electrons; indeed, they may have relatively high affinities to charges, holes in particular. Collectively, the charge affinity (i.e., inductive effect or inductive power) may be in the increasing order: *methylene*  $\approx$  *methyl*  $\approx$  *vinyl repeat unit* < *phenyl*  $\ll$  *methoxy* < *methylenedioxy* < *ester linker*. The second considerable factor is the resonance effect that functions to stabilize the trapped charges. Phenyl unit is well known to have two different resonance forms via  $\pi$ -conjugations. There are two different resonance forms (which include a charge-separated form) possible for ester unit. The other components have no resonance forms. Then, the resonance effect could be listed in the increasing order: *methylene*  $\approx$  *methyl*  $\approx$  *vinyl repeat unit*  $\approx$  *methoxy*  $\approx$  *methylenedioxy* < *ester linker*  $\ll$  *phenyl*. As a result, higher charge affinity and higher resonance effect have a synergistic correlation that positively impacts both the charge trapping capacity and the stabilization of trapped charges, a key aspect of developing memory polymers. Considering the two aforementioned factors, the charge trapping and charge stabilization power is in the increasing order: *methylene*  $\approx$  *methyl*  $\approx$  *vinyl repeat unit*  $\approx$  *methoxy*  $\approx$  *methylenedioxy* < *ester linker* < *phenyl* < *methylphenyl*  $\ll$  *monomethoxyphenyl* < *dimethoxyphenyl* < *methylenedioxyphenyl* < *trimethoxyphenyl* (Figure S25). This can be expanded to the overall charge trapping and stabilization

power of polymers in this study as the following increasing order: PEM-Bz  $\approx$  PEM-BzMe  $\ll$  PEM-BzOMe  $<$  PEM-BzOMe<sub>2</sub>  $\ll$  PEM-BzO<sub>2</sub>C  $<$  PEM-BzOMe<sub>3</sub>. Thus, no digital memory behaviors (i.e., dielectric characteristics) of PEM-Bz and PEM-BzMe might be attributed to the low charge affinities of their chemical components, in particular the phenyl and methylphenyl moieties. The DRAM behaviors of PEM-BzOMe and PEM-BzOMe<sub>2</sub> could be driven by the monomethoxyphenyl and dimethoxyphenyl moieties having intermediate levels of charge trapping and stabilization power. The WORM memory and DRAM behaviors of PEM-BzO<sub>2</sub>C and PEM-BzOMe<sub>3</sub> might originate from the 3,4-methylenedioxyphenyl and trimethoxyphenyl moieties having high levels of charge trapping and stabilization power. Here it is noted that PEM-BzO<sub>2</sub>C exhibits better digital memory performances (WORM memory, DRAM, and wider film thickness window) than PEM-BzOMe<sub>2</sub>. These results indicate that 3,4-methylenedioxyphenyl moiety exhibits relatively higher charge trapping and stabilization power than dimethoxyphenyl group. Overall, it can be rationalized that the phenyl unit having higher number of methoxy substituents behaves higher trapping and stabilization power to holes and eventually provide higher digital memory performances, namely more stable memory mode and wider film thickness window.

Here, one can raise another question: Why do all electroactive polymers of this study reveal film-thickness-dependent memory behaviors? In general, hopping conduction is widely adopted as a higher energy process in comparison to conduction processes in metallic conductors because of its hopping nature. The hopping nature may cause severe reductions in the charge mobility. The charge mobility may be further influenced by the charge trapping and stabilization power of locally-distributed electroactive moieties. Therefore, the observed thickness-dependent memory behaviors could be attributed mainly to the limited charge mobility due to the hopping conduction processes using the locally-distributed electroactive moieties. The charge mobility associated with higher charge trapping and stabilization power of electroactive moieties could lead wider thickness window of resistive memory behavior. The significance of the energy intensive nature of hopping process is evident in the case of PEM-BzO<sub>2</sub>C and PEM-BzOMe<sub>3</sub>, which exhibit film thickness-dependent memory mode changes. The 3,4-methylenedioxyphenyl and trimethoxyphenyl moieties have higher charge trapping and stabilization powers, compared to the other moieties. The high trapping and

stabilization powers could lead a more stable mode of digital memory (i.e., WORM memory) for film thickness up to around 20 nm. However, such trapping and stabilization powers might not be enough to continue revealing non-volatile memory for films thicker than 20 nm thickness. It turns out that the thickness-dependent memory mode changes are attributed to the hopping process nature associated with the limited charge trapping and stabilization powers and resulting charge mobilities.

#### 4. Conclusions

A series of new oxyphenyl-based polymers have been synthesized by the post-modification reactions of PEM with various oxybenzyl alcohol derivatives: PEM-BzOMe, PEM-BzOMe<sub>2</sub>, PEM-BzO<sub>2</sub>C, and PEM-BzOMe<sub>3</sub>. The polymers exhibit thermal stability up to 180 °C or higher temperatures. They are easily processed via conventional spin-coating and subsequent drying processes to produce amorphous high quality nanoscale films with low surface roughness. Their various properties have been characterized: glass transition temperature, electron and mass densities, molecular orbitals, and band gap.

All polymers successfully exhibit *p*-type unipolar resistive memory behaviors with low switching-ON voltages, high ON/OFF current ratios and high reliability. PEM-BzOMe and PEM-BzOMe<sub>2</sub> show only volatile memory characteristics whereas PEM-BzO<sub>2</sub>C and PEM-BzOMe<sub>3</sub> exhibit either non-volatile or volatile memory behaviors depending on the film thickness. In particular, these polymers showed memory behaviors over the exceptionally wide thickness window of <210 nm. The memory behaviors manifest through the combination of Schottky emission and trap-limited SCLC conductions in OFF-state and hopping conduction in ON-state using the locally-distributed electroactive moieties (i.e., oxyphenyl derivatives) as charge trap sites and stepping stones.

Overall, this study reports the first demonstration of the incorporation of electroactive oxyphenyl derivatives into polymers as a highly effective developmental strategy for designing high performance resistive memory materials. The modes (i.e., volatile and non-volatile) and working thickness window of resistive memory is shown to be highly controllable by tailoring the number of oxyphenyl units and/or oxy atomic components in the phenyl unit. PEM-BzO<sub>2</sub>C and PEM-BzOMe<sub>3</sub>

are the best candidates from this study for the low-cost mass production of *p*-type unipolar non-volatile and volatile high performing memory devices.

## ASSOCIATED CONTENT

### Supporting Information

The Supporting Information is available free of charge at <https://...>

Materials and synthesis; representative data and analyses of FTIR, <sup>1</sup>H NMR, SEC, TGA, DSC, GIWAXS, CV, UV spectrometry, *I-V* sweep.

## AUTHOR INFORMATION

### Corresponding Author

\*E-mail [satoh@eng.hokudai.ac.jp](mailto:satoh@eng.hokudai.ac.jp), Tel +81-11-706-6602, Fax +81-11-706-6602 (T.S).

### Author Contributions

T.S., T.I., and B.J.R. formulated the idea of the project. Design, synthesis, characterization, data analysis, and manuscript preparation was completed by B.J.R. All of the authors contributed to discussing the results and revising this manuscript.

### Notes

The authors declare no competing interests.

## ACKNOWLEDGEMENTS

This study was supported from the JSPS Grant-in-Aid for Scientific Research (B) (16H04152 and 19H02769 T.S.), the Photoexcitonic Project (Hokkaido University, T. S.), and the Frontier Chemistry Center (Hokkaido University, T. S. and T. I.). B. J. R. was funded by the JSPS Fellowship for Young Scientists.

## REFERENCES

1. Punie, Y. Learning Spaces: an ICT-enabled model of future learning in the Knowledge-based Society. *Eur. J. Education*, **2007**, *42*, 185–199.
2. Hilbert, M.; López, P. The World's Technological Capacity to Store, Communicate, and Compute Information *Science*, **2011**, *322*, 60–65.
3. Gantz, J. F.; Reinsel, D.; Rydning, J. The U.S. Datasphere: Consumers Flocking to Cloud, 2018. Seagate Web site. <https://www.seagate.com/files/www-content/our-story/trends/files/data-age-us-idc.pdf> (accessed April 15, 2019).

4. Semiconductor Industry Association, The International Technology Roadmap for Semiconductors 2.0, 2015. Semiconductor Industry Association Web site. [https://www.semiconductors.org/wp-content/uploads/2018/06/0\\_2015-ITRS-2.0-Executive-Report-1.pdf](https://www.semiconductors.org/wp-content/uploads/2018/06/0_2015-ITRS-2.0-Executive-Report-1.pdf)(accessed April 15, 2019).
5. Hasan, R. M. M.; Luo, X. Promising Lithography Techniques for Next-Generation Logic Devices, *Nanomanufacturing and Metrology*, **2018**, *1*, 67–81.
6. Service, R. F. Next-Generation Technology Hits an Early Midlife Crisis. *Science*, **2003**, *302*, 556–559.
7. Mikolajick, T.; Nagel, N.; Riedel, S.; Mueller, T.; Kuesters, K. H. Scaling of nonvolatile memories to nanoscale feature sizes. *Mater. Sci.-Pol.*, **2007**, *25*, 33–43.
8. Moore, G. E. Cramming More Components onto Integrated Circuits. *Proc. IEEE*, **1998**, *86*, 82–85.
9. Campañó, R. Trends in nanoelectronics. *Nanotechnology*, **2001**, *12*, 85–88.
10. Chen, W.-C. ed., *Electrical Memory Materials and Devices* [Online]; Royal Society of Chemistry, 2015. <https://pubs.rsc.org/en/content/ebook/978-1-78262-116-4> (accessed April 15, 2019).
11. Setter, N.; Damjanovic, D.; Eng, L.; Fox, G.; Gevorgian, S.; Hong, S.; Kingon, A.; Kohlstedt, H.; Park, N. Y.; Stephenson, G. B.; Stolitchnov, A. K.; Taganstev, D. V. T.; Yamada, T.; Streiffner, S. Ferroelectric thin films: Review of materials, properties, and applications. *J. Appl. Phys.*, **2006**, *100*, 051606.
12. De Boeck, J.; Van Roy, W.; Das, J.; Motsnyi, V.; Liu, Z.; Lagae, L.; Boeve, H.; Dessen, K.; Borghs, G. Technology and materials issues in semiconductor-based magnetoelectronics. *Semicond. Sci. Technol.*, **2002**, *17*, 342.
13. Hudgens, S.; Johnson, B. Overview of Phase-Change Chalcogenide Nonvolatile Memory Technology. *MRS Bull.*, **2004**, *29*, 829–832.
14. Hahm, S. G.; Ko, Y.-G.; Kwon, W.; Ree, M. Programmable digital polymer memories. *Curr. Opin. Chem. Eng.*, **2013**, *2*, 79–87.
15. Kurosawa, T.; Higashihara, T.; Ueda, M. Polyimide memory: a pithy guideline for future applications. *Polym. Chem.*, **2013**, *4*, 16–30.
16. Ling, Q.-D.; Liaw, D.-J.; Zhu, C.; Chan, D. S.-H.; Kang, E.-T.; Neoh, K.-G. Polymer electronic memories: materials, devices and mechanisms. *Prog. Polym. Sci.*, **2008**, *33*, 917–978.
17. Lin, W. P.; Liu, S. J.; Gong, T.; Zhao, Q.; Huang, W. Polymer-based resistive memory materials and devices. *Adv. Mater.*, **2014**, *26*, 570–606.
18. Yang, Y.; Ouyang, J.; Ma, L. P.; Tseng, R. J. H.; Chu, C. W. Electrical switching and bistability in organic/polymeric thin films and memory devices. *Adv. Funct. Mater.*, **2006**, *16*, 1001–1014.
19. Baek, S.; Lee, D.; Kim, J.; Hong, S.; Kim, O.; Ree, M. Novel digital nonvolatile memory devices based on semiconducting polymer thin films. *Adv. Funct. Mater.*, **2007**, *17*, 2637–2644.
20. Choi, S.; Hong, S.-H.; Cho, S. H.; Park, S.; Park, S.-M.; Kim, O.; Ree, M. High-Performance Programmable Memory Devices Based on Hyperbranched Copper Phthalocyanine Polymer Thin Films. *Adv. Mater.*, **2008**, *20*, 1766–1771.

21. Ko, Y.-G.; Kwon, W.; Kim, D. M.; Gal, Y.-S.; Ree, M. Programmable nonvolatile electrical memory characteristics of an ionic conjugated polymer. *Polym. Chem.*, **2012**, *3*, 2028–2033.
22. Nam, S.; Ko, Y.-G.; Hahm, S. G.; Park, S.; Seo, J.; Lee, H.; Kim, H.; Ree, M.; Kim, Y. Organic nonvolatile memory transistors with self-doped polymer energy well structures. *NPG Asia Mater.*, **2013**, *5*, e33.
23. Ko, Y.-G.; Kim, D. M.; Kim, K.; Jung, S.; Wi, D.; Michinobu, T.; Ree, M. Digital memory versatility of fully  $\pi$ -conjugated donor-acceptor hybrid polymers. *ACS Appl. Mater. Interfaces*, **2014**, *6*, 8415–8425.
24. Dong, L.; Li, G.; Yu, A.-D.; Bo, Z.; Liu, C.-L.; Chen, W.-C. Conjugated Donor-Acceptor-Acceptor (D-A-A) Molecule for Organic Nonvolatile Resistor Memory. *Chem. Asian J.*, **2014**, *9*, 3403–3407.
25. Lee, H.; Kim, Y.; Fukuta, S.; Kim, H.; Kim, Y.; Higashihara, T.; Ree, M. Nanoscale Film Morphology and n-Type Digital Memory Characteristics of  $\pi$ -Conjugated Donor-Acceptor Alternating Copolymer Based on Thiophene and Thiadiazole Units. *Macromol. Rapid Commun.*, **2019**, *40*, 1900005.
26. Hahm, S. G.; Lee, T. J.; Kim, D. M.; Kwon, W.; Ko, Y.-G.; Michinobu, T.; Ree, M. Electrical Memory Characteristics of Nitrogen-Linked Poly(2,7-carbazole)s. *J. Phys. Chem. C*, **2011**, *115*, 21954–21962.
27. Ling, Q.-D.; Chang, F.-C.; Song, Y.; Zhu, C.-X.; Liaw, D.-J.; Chan, D. S.-H.; Kang, E.-T.; Neoh, K.-G. Synthesis and dynamic random access memory behavior of a functional polyimide. *J. Am. Chem. Soc.*, **2006**, *128*, 8732–8733.
28. Hahm, S. G.; Choi, S.; Hong, S.-H.; Lee, T. J.; Park, S.; Kim, D. M.; Kwon, W.-S.; Kim, K.; Kim, O.; Ree, M. Novel Rewritable, Non-volatile Memory Devices Based on Thermally and Dimensionally Stable Polyimide Thin Film. *Adv. Funct. Mater.*, **2008**, *18*, 3276–3282.
29. Yu, A.-D.; Kurosawa, T.; Lai, Y.-C.; Higashihara, T.; Ueda, M.; Liu, C.-L.; Chen, W.-C. Flexible polymer memory devices derived from triphenylamine–pyrene containing donor–acceptor polyimides. *J. Mater. Chem.*, **2012**, *22*, 20754–20763.
30. Lee, T. J.; Ko, Y.-G.; Yen, H.-J.; Kim, K.; Kim, D. M.; Kwon, W.; Hahm, S. G.; Liou, G.-S.; Ree, M. Programmable digital nonvolatile memory behaviors of donor–acceptor polyimides bearing triphenylamine derivatives: effects of substituents. *Polym. Chem.*, **2012**, *3*, 1276–1283.
31. Ko, Y.-G.; Kwon, W.; Yen, H.-J.; Chang, C.-W.; Kim, D. M.; Kim, K.; Hahm, S. G.; Lee, T. J.; Liou, G.-S.; Ree, M. Various Digital Memory Behaviors of Functional Aromatic Polyimides Based on Electron Donor and Acceptor Substituted Triphenylamines. *Macromolecules*, **2012**, *45*, 3749–3758 (2012).
32. Chen, C.-J.; Yen, H.-J.; Chen, W.-C.; Liou, G.-S. Resistive switching non-volatile and volatile memory behavior of aromatic polyimides with various electron-withdrawing moieties. *J. Mater. Chem.*, **2012**, *22*, 14085–14093.
33. Kim, K.; Fang, Y.-K.; Kwon, W.; Pyo, S.; Chen, W.-C.; Ree, M. Tunable electrical memory characteristics of brush copolymers bearing electron donor and acceptor moieties. *J. Mater. Chem. C*, **2013**, *1*, 4858–4868.
34. Ko, Y.-G.; Hahm, S. G.; Murata, K.; Kim, Y. Y.; Ree, B. J.; Song, S.; Michinobu, T.; Ree, M. New fullerene-based polymers and their electrical memory characteristics. *Macromolecules*, **2014**, *47*, 8154–8163.

35. Park, S.; Kim, K.; Kim, D. M.; Kwon, W.; Choi, J.; Ree, M. High Temperature Polyimide Containing Anthracene Moiety and Its Structure, Interface, and Nonvolatile Memory Behavior. *ACS Appl. Mater. Interf.*, **2011**, *3*, 765–773.
36. Hahm, S. G.; Kang, N.-G.; Kwon, W.; Kim, K.; Ko, Y.-G.; Ahn, S.; Kang, B.-G.; Chang, T.; Lee, J.-S.; Ree, M. Programmable bipolar and unipolar nonvolatile memory devices based on poly(2-(*N*-carbazolyl)ethyl methacrylate) end-capped with fullerene. *Adv. Mater.*, **2012**, *24*, 1062–1066.
37. Sun, H.-S.; Chiu, Y.-C.; Chen, W.-C. Renewable polymeric materials for electronic applications. *NPG Polymer J.*, **2017**, *49*, 61–73.
38. Kim, Y.; Song, S.; Liaw, D.-J.; Huang, Y.-C.; Ko, Y.-G.; Ihm, K.; Kim, J.; Ree, M. Digital Memory Characteristics of Aromatic Polyimides Based on Pyridine and Its Derivatives. *ACS Omega*, **2018**, *3*, 13036–13044.
39. Lee, J.; Kim, Y.; Kim, C.; Ree, M. New high performance digital memory devices fabricated with DNA and DNA-mimics. *Materials Horizon*, **2017**, *4*, 423–430.
40. Hahm, S. G.; Park, S.; Ko, Y.-G.; Ree, M. New photopatternable polyimide and programmable nonvolatile memory performances. *NPG Asia Materials*, **2017**, *9*, e374.
41. Song, S.; Ko, Y.-G.; Lee, H.; Wi, D.; Ree, B. J.; Li, Y.; Michinobu, T.; Ree, M. High-performance triazole-containing brush polymers via azide–alkyne click chemistry: a new functional polymer platform for electrical memory devices. *NPG Asia Materials*, **2015**, *7*, e228.
42. Kim, Y. Y.; Ree, B. J.; Kido, M.; Ko, Y.-G.; Ishige, R.; Hirai, T.; Wi, D.; Kim, J.; Kim, W. J.; Takahara, A.; Ree, M. High-Performance n-Type Electrical Memory and Morphology-Induced Memory-Mode Tuning of a Well-Defined Brush Polymer Bearing Perylene Diimide Moieties. *Adv. Electronic Mater.*, **2015**, *1*, 1500197.
43. Ree, B. J.; Kwon, W.; Kim, K.; Ko, Y.-G.; Kim, Y. Y.; Lee, H.; Ree, M. Clues to the Electrical Switching Mechanism of Carbazole-Containing Polyimide Thin Films. *ACS Appl. Mater. Interf.*, **2014**, *6*, 21692–21701.
44. Ko, Y.-G.; Hahm, S. G.; Murata, K.; Kim, Y. Y.; Ree, B. J.; Song, S.; Michinobu, T.; Ree, M. New Fullerene-Based Polymers and Their Electrical Memory Characteristics. *Macromolecules*, **2014**, *47*, 8154–8163.
45. Kim, K.; Kim, Y. Y.; Park, S.; Ko, Y.-G.; Rho, Y.; Kwon, W.; Shin, T. J.; Kim, J.; Ree, M. Nanostructure- and Orientation-Controlled Digital Memory Behaviors of Linear-Brush Diblock Copolymers in Nanoscale Thin Films. *Macromolecules*, **2014**, *47*, 4397–4407.
46. Kwon, W.; Rho, Y.; Kamoshida, K.; Kwon, K. H.; Jeong, Y. C.; Kim, J.; Misaka, H.; Shin, T. J.; Kim, J.; Kim, K.-W.; Jin, K. S.; Chang, T.; Kim, H.; Satoh, T.; Kakuchi, T.; Ree, M. Well-Defined Functional Linear Aliphatic Diblock Copolyethers: A Versatile Linear Aliphatic Polyether Platform for Selective Functionalizations and Various Nanostructures. *Adv. Funct. Mater.*, **2012**, *22*, 5194–5208.
47. Ree, B. J.; Kobayashi, S.; Heo, K.; Lee, T. J.; Satoh, T.; Ishizone, T.; Ree, M. Nanoscale Film Morphology and Property Characteristics of Dielectric Polymers Bearing Monomeric and Dimeric Adamantane Units. *Polymer*, **2019**, *169*, 225–233.
48. Yoon, J.; Kim, K.-W.; Kim, J.; Heo, K.; Jin, K. S.; Jin, S.; Shin, T. J.; Lee, B.; Rho, Y.; Ahn, B.; Ree, M. Small-Angle X-ray Scattering Station 4C2 BL of Pohang Accelerator Laboratory for Advance in Korean Polymer Science. *Macromol. Res.*, **2008**, *16*, 575–585.

49. Kim, Y. Y.; Jung, S.; Kim, C.; Ree, B. J.; Kawato, D.; Nishikawa, N.; Suemasa, D.; Isono, T.; Kakuchi, T.; Satoh, T.; Ree, M. Hierarchical Structures in Thin Films of Miktoarm Star Polymers: Poly(n-hexyl isocyanate)(12K)–Poly( $\epsilon$ -caprolactone)<sub>1–3</sub>(5K). *Macromolecules*, **2014**, *47*, 7510–7524.
50. Lee, B.; Park, Y.-H.; Hwang, Y.; Oh, W.; Yoon, J.; Ree, M. Ultralow-k Nanoporous Organosilicate Dielectric Films Imprinted with Dendritic Spheres. *Nat. Mater.*, **2005**, *4*, 147–150.
51. Kim, Y. Y.; Ree, B. J.; Kido, M.; Ko, Y.-G.; Ishige, R.; Hirai, T.; Wi, D.; Kim, J.; Kim, W. J.; Takahara, A.; Ree, M. High-Performance n-Type Electrical Memory and Morphology-Induced Memory-Mode Tuning of a Well Defined Brush Polymer Bearing Perylene Diimide Moieties. *Adv. Electron. Mater.*, **2015**, *1*, 1500197.
52. Bolze, J.; Kim, J.; Huang, J.-Y.; Rah, S.; Youn, H. S.; Lee, B.; Shin, T. J.; Ree, M. Current Status of the Synchrotron Small-Angle X-Ray Scattering Station BL4C1 at the Pohang Light Source. *Macromol. Res.*, **2002**, *10*, 2–12.
53. Park, B.-J.; Rah, S.-Y.; Park, Y.-J.; Lee, K.-B. PLS Bending Magnet X-Ray Beamline 3C2. *Rev. Sci. Instrum.*, **1995**, *66*, 1722–1724.
54. Parratt, L. G. Surface Studies of Solids by Total Reflection of X-Rays. *Phys. Rev.*, **1954**, *95*, 359–369.
55. Bolze, J.; Ree, M.; Youn, H. S.; Chu, S.-H.; Char, K. Synchrotron X-ray Reflectivity Study on the Structure of Templated Polyorganosilicate Thin Films and Their Derived Nanoporous Analogues. *Langmuir*, **2001**, *17*, 6683–6691.
56. Schottky, W. Über den Austritt von Elektronen aus Glühdrähten bei verzögernden Potentialen. *Ann. Physik*, **1914**, *44*, 1011–1032.
57. Sze, S. M.; Crowell, C. R.; Kahng, D. Photoelectric Determination of the Image Force Dielectric Constant For Hot Electrons in Schottky Barriers. *J. Appl. Phys.*, **1964**, *35*, 2534–2536.
58. Crowell, C. R. The Richardson constant for thermionic emission in Schottky barrier diodes. *Solid-State Electron.*, **1965**, *8*, 395–399.
59. Campbell, A. J.; Bradley, D. D. C.; Lidzey, D. G. Space-charge limited conduction with traps in poly(phenylene vinylene) light emitting diodes. *J. Appl. Phys.*, **1997**, *82*, 6326–6342.
60. Mark, P.; Helfrich, W. Space-Charge-Limited Currents in Organic Crystals. *J. Appl. Phys.*, **1962**, *33*, 205–215.
61. Hill, R. M. Variable-Range Hopping. *Physica Status Solidi A*, **1976**, *34*, 601–613.
62. Paasch, G.; Lindner, T.; Scheinert, S. Variable range hopping as possible origin of a universal relation between conductivity and mobility in disordered organic semiconductors. *Synthetic Metals*, **2002**, *132*, 97–104.
63. Ohm, G. S. *The Galvanic Circuit Investigated Mathematically*; Creative Media Partners, LLC, 2015.

## Graphical Abstract for the Table of Contents

# Chemically Controlled Volatile and Nonvolatile Resistive Memory Characteristics of Novel Oxygen-based Polymers

Brian J. Ree, Takuya Isono, and Toshifumi Satoh\*

This study demonstrated for the first time that the chemical incorporation of oxyphenyl derivatives into dielectric polymers as electroactive moieties is a very powerful development route of high performance digital memory materials. Oxyphenyl-based polymers in nanoscale films exhibit volatile and non-volatile digital memories with low power consumption, high ON/OFF current ratios and high reliability; higher number of oxy substituents in the phenyl unit could lead permanent memory (which is the most stable memory mode) and much wider thickness window. They are suitable for the low-cost mass production of *p*-type permanent and volatile memory devices with high performances.

